Chapter-6

ACOUSTIC STABILITY OF ASTROPHYSICAL GYROMAGNETOACTIVE VISCOUS CYLINDRICAL PLASMAS

Abstract: *In the present Chapter we employ a quantum hydrodynamic model to investigate the cylindrical acoustic waves excited in a gyromagnetoactive self-gravitating viscous cylinder of electron-ion plasma*[†]*. The electronic equation of state incorporates the effect of temperature degeneracy resulting in the completely degenerate Fermi quantum pressure and the completely non-degenerate classical pressure. The constitutive ions are governed by the appropriate equation of state (classical). A standard cylindrical normal mode analysis employing the Hankel function procedurally yields a generalized linear sextic dispersion relation. The low-frequency analysis is carried out in four distinct parametric special cases of astronomical importance. It includes the quantum (completely degenerate) non-planar (cylindrical), quantum (completely degenerate) planar, classical (completely non-degenerate) non-planar (cylindrical), and classical (completely non-degenerate) planar. A numerical illustrative platform is provided to investigate the stability patterns with multiparametric variations, such as the number density, Coriolis rotation, magnetic field, etc. The astronomical circumstances of our analysis are finally highlighted.*

6.1 INTRODUCTION

The study of acoustic waves and instabilities excitable in two-component plasmas (electron-ion) has recently gathered significant research interest because of their large-scale applications in explorative areas in both the classical and quantum regimes. Such plasmas are naturalistically ubiquitous in diverse circumstances. It mainly includes inertially confined laboratory plasmas, liquid metals, stellar and planetary interiors, Earth's auroral regions, Jupiter magnetosphere, supernova explosions, and so on [1-6]. As a consequence, it is quite expedient to analyze the supported normal acoustic waves and instabilities to perceive their bulk stability behaviours in various realistic astronomical circumstances.

[†]Dasgupta, S., Atteya, A. and Karmakar, P. K. Acoustic stability of a self-gravitating cylinder leading to astrostructure formation. *Scientific Reports*, 13: 7163, 2023.

Several investigations to study the dynamics of acoustic waves and instabilities in both planar and non-planar geometries in astrophysical plasmas have already been reported in the literature [7-23]. It is clearly evident now that, even though there are quite a large number of studies dealing with acoustic waves in cylindrical and spherical geometries, the cylindrical acoustic modal analysis by employing the Hankel function formalism in realistic astronomical circumstances is yet to be performed to the best of our knowledge. In other words, study of cylindrical acoustic wave-instability problems by means of the Hankel function formalism [24] in a uniformly rotating magnetized plasma system in both planar and non-planar geometric configurations is still an open problem hitherto lying unexplored in the context of understanding astronomical disc stability, filamentary astrostructures, etc.

In the present semi-analytic investigation, we consider a generalized quantum two-component hydrodynamic model in cylindrical geometry on the astronomical spatiotemporal scales. This electron-ion plasma is confined in a magnetized axisymmetric cylinder rotating uniformly about the reference axis (longitudinal). The electrons and ions are governed by their appropriate equations of state. The fermions governed by the Fermi-Dirac statistical distribution law are characterized by temperature (T) and chemical potential (μ) [25-27]. The effect of temperature degeneracy considered here is incorporated in the electronic equation of state with the help of the temperature degeneracy parameter given as, $G_e' = Li_{5/2}(-\xi)/Li_{3/2}(-\xi)$, where $\xi(\mu,T) = e^{\beta\mu}$ and $\beta = 1/k_B T$ [25-27]. The electronic equation of state results in the completely degenerate quantum pressure (Fermi) and the completely non-degenerate classical pressure (thermal) in the light of appropriate approximations. The ionic equation of state takes into account the classical thermal pressure. A standard normal cylindrical wave analysis by employing the Hankel function [24] yields a sextic dispersion relation, which is then analyzed in the low-frequency regime. The modified dispersion relation is then investigated in the light of four different parametric windows. We study the influence of various realistic parameters on the instability dynamics, such as equilibrium number density, kinematic viscosity, and so forth. The importance of cylindrical geometry considered here can be justified from the fact that axisymmetric cylinders under self-gravity offer significant insights on the evolution of elongated

molecular cloud, magnetized arms of spiral galaxies, circumnuclear starburst rings, and filamentary structures in diverse astronomic and cosmological environs [28-30].

6.2 PHYSICAL MODEL AND FORMALISM

We consider a magnetized axisymmetric cylindrical two-component plasma system subjected to the non-local self-gravitational action. It consists of electrons and singly charged ions. The former is judiciously modelled with the help of generalized quantum hydrodynamic formalism; whereas, the latter is treated classically. This model evolves under the conjoint influence of the Lorentz force, Coriolis rotation, kinematic viscosity, Bohm potential, and temperature degeneracy effects. The confining cylinder rotates with a constant angular velocity directed along the longitudinal direction. The basic governing equations here consist of continuity equation, force-balancing momentum equation, and appropriate equation of state. The system closure is obtained with the help of electrostatic and gravitational Poisson equations. The quantum dynamics of the electronic species in generic notations is accordingly cast as

$$\partial_t n_e + (r)^{-1}\partial_r\left(r n_e u_e\right) = 0\,, \tag{6.1}$$

$$\partial_t u_e = \left(e m_e^{-1}\right)\partial_r \phi_E - e B_z m_e^{-1} u_{e\phi} + \left(m_e n_e^{-1}\right)\partial_r P_e + \hbar^2\left(2m_e^2\right)^{-1}\partial_r n_e^{-1/2}\left\{r^{-1}\partial_r\left(r n_e^{1/2}\right)\right\} + 2v_\phi\omega_z - \partial_r\psi\,, \tag{6.2}$$

$$P_e = G_e^{'} n_e \beta^{-1}\,. \tag{6.3}$$

Likewise, the classical dynamics of the ionic species is described as

$$\partial_t n_i + (r)^{-1}\partial_r\left(r n_i u_i\right) = 0\,, \tag{6.4}$$

$$\partial_t u_i = \left(e m_i^{-1}\right)\partial_r \phi_E - e B_z m_i^{-1} u_{i\phi} + \left(m_i n_i\right)^{-1}\partial_r P_i + 2v_\phi\omega_z + \left(m_i n_i\right)^{-1}\eta(r)^{-1}\partial_r\left(r\partial_r u_i\right) - \partial_r\psi\,, \tag{6.5}$$

$$P_i = n_i k_B T\,. \tag{6.6}$$

The model is systematically closed with the help of electrostatic and self-gravitational Poisson equations given respectively in customary notations as

$$(r)^{-1}\partial_r\left(r\partial_r\phi_E\right)=e\left(\varepsilon_0^{-1}\right)\left(n_e-n_i\right), \tag{6.7}$$

$$(r)^{-1}\partial_r\left(r\partial_r\psi\right)=4\pi G\left(\Delta\rho_e+\Delta\rho_i\right). \tag{6.8}$$

Here, we consider a cylindrical coordinate system where r and t denote the spatial and temporal parameters, respectively. $n_{e(i)}$ and $u_{e(i)}$, denote the population density and the velocity of the electrons (ions) with their inertial mass $m_{e(i)}$, respectively. $\omega_{ge(i)}=eB_z/m_{e(i)}$ is the electronic (ionic) magnetic gyrofrequency, where B_z is the magnetic field acting along the longitudinal direction. The axisymmetric plasma system is assumed to be rotating with a constant angular velocity ω. The constant rotational force acting on the entire system is given by $C_F^*=2v_\phi\omega_z$, where ω_z is the longitudinal component of the angular velocity and v_ϕ is the azimuthal component of linear velocity. $P_{e(i)}$ gives the pressure acting on the electronic (ionic) species. $h=6.6\times10^{-34}$ J s is the Planck constant. T is the thermal temperature. $k_B=1.38\times10^{-23}$ J K^{-1} is the Boltzmann constant. ϕ_E and ψ are the electrostatic potential and gravitational potential, respectively. $\varepsilon_0=8.85\times10^{-12}$ F m^{-1} is the permittivity of free space. $G=6.67\times10^{-11}$ N m^2 kg^{-2} is the universal gravitational constant. In equation (6.8), $\Delta\rho_{e(i)}=\rho_{e(i)}-\rho_0=m_{e(i)}\left(n_{e(i)}-n_0\right)$ is used to model the so called Jeans swindle as a self-gravitational homogenization tool.

A number of physical points regarding the above mathematical equations are noteworthy. Here, equation (6.1) is the equation of continuity, depicting the flux conservation of the electronic fluid. Then, equation (6.2) is the force balancing (momentum) equation. Here, the force by virtue of electronic motion (L.H.S) is balanced by the forces arising due to electrostatic potential (1st term in R.H.S), magnetic field (2nd term in R.H.S), electronic pressure (3rd term in R.H.S), quantum Bohm potential (4th term in R.H.S), Coriolis rotation (5th term in R.H.S), and gravitational potential (6th term in R.H.S). The electronic equation of state incorporating the

temperature degeneracy effects is represented by equation (6.3). The arbitrary temperature degeneracy in usual notations [25-27] is given as $G_e' = Li_{5/2}(-\xi)/Li_{3/2}(-\xi)$. Here, $Li_p(-\xi)$ is the polylogarithmic function with index p. $\xi(\mu,T) = e^{\beta\mu} = e^{\mu/k_B T}$ describes the degeneracy of the system [25-27]. The general form of $Li_p(-\xi)$ for $p>0$ is given as

$$Li_p(-\xi) = -(\Gamma(p))^{-1}\int_0^\infty t^{p-1}\left(e^t\xi^{-1}+1\right)^{-1}dt\,; \tag{6.9}$$

where, $\Gamma(p) = \int_0^\infty x^{p-1}e^{-x}\,dx$ is the gamma function with argument p.

For the completely degenerate limit ($\xi \to \infty$), one gets

$$G_e' = 2(5\delta)^{-1}, \tag{6.10}$$

$$P_e = \left(3\pi^2\right)^{2/3}\hbar^2 n_e^{5/3}(5m_e)^{-1} \tag{6.11}$$

where, $\delta = T/T_F$ denotes the ratio between the thermal and Fermi temperature;

For the completely non-degenerate limit ($\xi \to 0$), one gets

$$G_e' = 1\ , \tag{6.12}$$

$$P_e = n_e k_B T\ . \tag{6.13}$$

It is evident that equation (6.4) is the ionic analog of equation (6.1). Likewise, equation (6.5) is the exact analog of equation (6.2), except the Bohm potential term, since the ions are treated classically because of their large mass. The ionic fluid is characterized with the kinematic viscosity (5^{th} term in R.H.S), in addition to all the forces already mentioned before in the case of equation (6.3). Now, equation (6.6) is the ionic equation of state modelled classically. The model closure is obtained with the help of electrostatic and gravitational Poisson equations (equations (6.7), (6.8)).

For a scale-invariant analysis, we adopt a standard astronormalization scheme [20]. The corresponding normalized sets of equations are cast as

$$\partial_\tau N_e + (R)^{-1}\partial_R(RN_eM_e) = 0\,, \tag{6.14}$$

$$\begin{aligned} &N_e\partial_\tau M_e = (m_i m_e^{-1})N_e\partial_R\Phi_E - N_e\Omega^*_{ge}M_{e\phi} + 3^{-1}M^2_{Fe}\partial_R N_e \\ &+ 4^{-1}H_p^2\{\partial_R^3 N_e + (R^{-1})\partial_R^2 N_e - (R^{-2})\partial_R N_e\} \\ &+ 2N_eM_\phi\omega_z^* - N_e\partial_R\Psi \qquad \text{(for completely degenerate case)}, \end{aligned} \tag{6.15.1}$$

$$\begin{aligned} &N_e\partial_\tau M_e = (m_i m_e^{-1})N_e\partial_R\Phi_E - N_e\Omega^*_{ge}M_{e\phi} + (m_i m_e^{-1})\partial_R(N_eT^*) \\ &+ 2N_eM_\phi\omega_z^* - N_e\partial_R\Psi \ \text{(for completely non-degenerate case)}, \end{aligned} \tag{6.15.2}$$

$$\partial_\tau N_i + (R)^{-1}\partial_R(RN_iM_i) = 0\,, \tag{6.16}$$

$$N_i\partial_\tau M_i = -N_i\partial_R\Phi_E + N_i\Omega^*_{gi}M_{i\phi} + \partial_R(N_iT^*) + 2N_iM_\phi\omega_z^* + \eta^*(R)^{-1}\partial_R(R\partial_R M_i) - N_i\partial_R\Psi\,, \tag{6.17}$$

$$(R)^{-1}\partial_R(R\partial_R\Phi_E) = (N_e - N_i)\,, \tag{6.18}$$

$$(R)^{-1}\partial_R(R\partial_R\Psi) = \sigma\{m_e m_i^{-1}(N_e - 1) + (N_i - 1)\}. \tag{6.19}$$

In the above equations (6.14)-(6.19), the spatial coordinate r is normalized as $R = r/L_0$; where, $L_0 = c_s/\omega_{pi}$ is a characteristic spatial scale. $c_s = \sqrt{2E_{Fe}/m_i} = hn_0/4\sqrt{m_e m_i}$ is the acoustic speed in terms of Fermi energy. $\omega_{pi} = \sqrt{n_0 e^2/\varepsilon_0 m_i}$ designates the ion plasma oscillation frequency. The temporal coordinate t is normalized as $\tau = t/\omega_{pi}^{-1}$. The Fermi energy is given as $E_{Fe} = p_F^2/2m_e$, with $p_F = hn_0/4$ as the corresponding Fermi momentum. The rescaled electronic (ionic) number density is given as $N_{e(i)} = n_{e(i)}/n_0$, where n_0 is the equilibrium number density. $M_{e(i)} = u_{e(i)}/c_s$ gives the Mach number of the electronic (ionic) species. The normalized

electronic (ionic) magnetic gyrofrequency is given as $\Omega^*_{ge(i)}=\omega_{ge(i)}/\omega_{pi}$. The normalized Coriolis rotational force is given as $C^*_F = M_\phi \omega^*_z$; where, $M_\theta = v_\phi / c_s$ is the rescaled tangential velocity of the system and $\omega^*_z = \omega_z/\omega_{pi}$ is the rescaled longitudinal component of angular velocity. $M_{Fe} = v_{Fe}/c_s$ is the Fermi Mach number, where, v_{Fe} is the Fermi velocity. $H_p = \hbar\omega_{pi}/m_e c_s^2$ is the quantum parameter. $\sigma = \omega_{Ji}^2/\omega_{pi}^2$ gives the ratio of the squares of Jeans frequency to that of ionic plasma oscillation frequency. $\omega_{Ji} = \sqrt{4\pi G m_i n_0}$ gives the Jeans frequency for ions. The normalized kinematic viscosity is given as $\eta^* = \eta/m_i n_0 c_s L_0$. $T^* = Tk_B/m_i c_s^2$ gives the normalized temperature. In a similar pattern, $\Phi_E = e\phi_E/2E_{Fe}$ is the normalized electrostatic potential. The normalized gravitational potential is given as $\Psi = \psi/c_s^2$.

It is to be noted that in the quantum regime, Bohm potential term accounts for the typical quantum like behaviour like tunneling, overlapping of wave packets, and so on. Thus in the completely non-degenerate (classical) regime represented by equation (6.15.2), normalized Bohm potential term is ignored [31, 32].

6.3 LINEAR STABILITY ANALYSIS

We linearly perturb the relevant physical fluid parameters appearing in equations (6.14)-(6.19), using a cylindrical wave analysis [24] in an autonormalized Fourier transformed wavespace given as

$$F(R,\tau) = F_0 + F_1(R,\tau) = F_0 + F_{10}\exp(-i\Omega\tau)H_0^{(1)}(k^*R), \tag{6.20}$$

where $H_0^{(1)}$ is the Hankel function of the first kind, of order 0.

For $R \to 0$, $H_0^{(1)}$ has logarithmic singularity:

$$H_0^{(1)} = (2i\pi^{-1})\log(k^*R) \tag{6.21}$$

At large distances, we have

$$H_0^{(1)} = \left(2\pi^{-1}\right)^{1/2}\left(k^* R\right)^{-1/2}\exp\left[i\left(k^* R - \pi 4^{-1}\right)\right]. \tag{6.22}$$

Thus, equation (6.20) gets modified as

$$F(R,\tau) = F_0 + F_1(R,\tau) = F_0 + F_{10}\left(2\pi^{-1}\right)^{1/2}\left(k^* R\right)^{-1/2}\exp\left[i\left(k^* R - \Omega\tau - \pi 4^{-1}\right)\right], \tag{6.23}$$

$$F = \left[N_s \quad M_s \quad \Phi_E \quad \Psi\right]^T, \tag{6.24}$$

$$F_0 = \left[1 \quad 0 \quad 0 \quad 0\right]^T, \tag{6.25}$$

$$F_1 = \left[N_{s1} \quad M_{s1} \quad \Phi_{E1} \quad \Psi_1\right]^T. \tag{6.26}$$

Here, we assume an axisymmetric cylinder such that all quantities are homogeneously distributed along z-direction, and thereby just show radial variations. In equation (6.23), F_1 denotes the radial perturbations, which evolve as per the Hankel function of first kind of order 0. F_0 denotes the equilibrium values corresponding to which perturbations F_1 take place. In the new Fourier transformed wavespace, the spatial and temporal operators get transformed as $\partial/\partial R \to \left(ik^* - 1/R\right)$ and $\partial/\partial\tau \to (-i\,\Omega)$, respectively. Here, Ω $\left(=\omega/\omega_{pi}\right)$ denotes the normalized fluctuation frequency and $k^*\left(\sim k/L_0^{-1}\right)$ designates the normalized wavenumber. The linearly perturbed relevant physical parameters from equations (6.14)-(6.19) in the new wave space can respectively be cast as

$$N_{e1} = -i\Omega^{-1}\left\{ik^* + (2R)^{-1}\right\}M_{e1}, \tag{6.27}$$

$$M_{e1} = E^{-1}\left(m_i m_e^{-1}\right)\left\{ik^* - (2R)^{-1}\right\}\Phi_{E1} - iE^{-1}\Omega^{-1}\sigma\left\{k^{*2} + \left(4R^2\right)^{-1}\right\}\left\{-k^{*2} + \left(4R^2\right)^{-1}\right\}^{-1}M_{i1}, \tag{6.28}$$

$$N_{i1} = -i\Omega^{-1}\left\{ik^* + (2R)^{-1}\right\}M_{i1}, \tag{6.29}$$

$$M_{i1} = -H^{-1}\left\{ik^{*} - (2R)^{-1}\right\}\Phi_{E1}\left[1 + i\Omega^{-1}E^{-1}\sigma\left\{k^{*^2} + \left(4R^2\right)^{-1}\right\}\left\{-k^{*^2} + \left(4R^2\right)^{-1}\right\}^{-1}\right], \quad (6.30)$$

$$\Phi_{E1} = -i\Omega^{-1}\left\{ik^{*} + (2R)^{-1}\right\}\left\{-k^{*^2} + \left(4R^2\right)^{-1}\right\}^{-1}\left(M_{e1} - M_{i1}\right), \quad (6.31)$$

$$\Psi_1 = -i\Omega^{-1}\sigma\left\{ik^{*} + (2R)^{-1}\right\}\left\{-k^{*^2} + \left(4R^2\right)^{-1}\right\}^{-1}\left\{\left(m_e m_i^{-1}\right)M_{e1} + M_{i1}\right\}. \quad (6.32)$$

In the above set of equations (6.27)-(6.32), the various substituted terms are given as

$$E = -i\Omega + i\Omega^{-1}\left\{ik^{*} + (2R)^{-1}\right\}\left[-\Omega_{ge}^{*}M_{e\phi} + 4^{-1}H_p^2 B_p + 2M_{\phi}\omega_z^{*}\right.$$
$$\left. + \left\{ik^{*} - (2R)^{-1}\right\}\left[\alpha - \left\{-k^{*^2} + \left(4R^2\right)^{-1}\right\}^{-1}\sigma m_e m_i^{-1}\right]\right], \quad (6.33)$$

$$B_p = -ik^{*^3} + k^{*^2}(2R)^{-1} + ik^{*}\left(4R^2\right)^{-1} - 5\left(8R^3\right)^{-1}, \quad (6.34)$$

$\alpha = (3)^{-1}M_{Fe}^2$, for completely degenerate case; $M_{Fe} = v_{Fe}/c_s$ and $v_{Fe} = \left(3\pi^2 n_e\right)^{1/3}\hbar m_e^{-1}$, (6.35)

$\alpha = m_i m_e^{-1}T^{*}$, for completely non-degenerate case (6.36)

$$H = -i\Omega + i\Omega^{-1}\left\{ik^{*} + (2R)^{-1}\right\}\left[\Omega_{gi}^{*}M_{i\phi} + 2M_{\phi}\omega_z^{*} + \left\{ik^{*} - (2R)^{-1}\right\}\left[T^{*} - \sigma\left\{-k^{*^2} + \left(4R^2\right)^{-1}\right\}^{-1}\right]\right]$$
$$-\left\{-k^{*^2} + \left(4R^2\right)^{-1}\right\}\eta^{*} + \Omega^{-2}\left\{k^{*^2} + \left(4R^2\right)^{-1}\right\}^2\left\{-k^{*^2} + \left(4R^2\right)^{-1}\right\}^{-2}\sigma^2 m_e m_i^{-1}E^{-1} \quad (6.37)$$

After a standard procedure of elimination and substitution among equations (6.27)-(6.37), we obtain a generalized linear sextic dispersion relation cast as

$$\Omega^6 + A_5\Omega^5 + A_4\Omega^4 + A_3\Omega^3 + A_2\Omega^2 + A_1\Omega + A_0 = 0. \quad (6.38)$$

The different coefficients in an expanded form are given as

$$A_5 = -i\left\{k^{*^2} + \left(4R^2\right)^{-1}\right\}\eta^*, \tag{6.39}$$

$$A_4 = \left\{ik^* + (2R)^{-1}\right\}\left[-2\Omega_{ge}^* M_{e\phi}^* + \left(2\alpha + T^*\right)\left\{ik^* - (2R)^{-1}\right\} - 2^{-1}H_p^2 B_p + 6M_\phi\omega_z^* + \Omega_{gi}^* M_{i\phi}^*\right.$$
$$\left. + \left\{ik^* - (2R)^{-1}\right\}\left\{-k^{*^2} + \left(4R^2\right)^{-1}\right\}^{-1}\left\{m_i m_e^{-1} + 1 - \sigma\left(2m_e m_i^{-1} + 1\right)\right\}\right], \tag{6.40}$$

$$A_3 = -i\left\{ik^* + (2R)^{-1}\right\}\eta^*\left[\left\{-k^{*^2} + \left(4R^2\right)^{-1}\right\}\left[2\Omega_{ge}^* M_{e\phi}^* + 2^{-1}H_p^2 B_p - 4M_\phi\omega_z^* - 2\alpha\left\{ik^* - (2R)^{-1}\right\}\right]\right.$$
$$\left. + \left\{ik^* - (2R)^{-1}\right\}\left(2\sigma m_e m_i^{-1} - m_i m_e^{-1}\right)\right], \tag{6.41}$$

$$A_2 = -\left\{ik^* + (2R)^{-1}\right\}^2\left[\left\{ik^* - (2R)^{-1}\right\}\left[-2\alpha\left(\Omega_{ge}^* M_{e\phi}^* - \Omega_{gi}^* M_{i\phi}^*\right) + 2^{-1}H_p^2 B_p\alpha + 4M_\phi\omega_z^*\left(\alpha + T^*\right)\right.\right.$$
$$\left. - 2\left(\Omega_{ge}^* M_{e\phi}^* T^* - 2M_\phi\omega_z^*\alpha\right) - 2^{-1}T^* H_p^2 B_p + \left\{-k^{*^2} + \left(4R^2\right)^{-1}\right\}^{-1}\left[2\Omega_{ge}^* M_{e\phi}\sigma\left(1 + m_e m_i^{-1}\right)\right.\right.$$
$$\left. - 2^{-1}H_p^2 B_p\sigma\left(-1 + m_e m_i^{-1}\right) - 2\sigma\left\{\left(\Omega_{gi}^* M_{i\phi} + 4M_\phi\omega_z^*\right)m_e m_i^{-1} + 2M_\phi\omega_z^*\right\} + 2\left\{\Omega_{ge}^* M_{e\phi} + 2M_\phi\omega_z^*\right.\right.$$
$$\left.\left. - 4^{-1}H_p^2 B_p\right\} + m_i m_e^{-1}\left(\Omega_{gi}^* M_{i\phi} + 4M_\phi\omega_z^* - \Omega_{ge}^* M_{e\phi} + 4^{-1}H_p^2 B_p\right)\right]\left.\right] + \left\{ik^* - (2R)^{-1}\right\}^2\left[\alpha^2\right.$$
$$\left. + 2\alpha T^* + \left\{-k^{*^2} + \left(4R^2\right)^{-1}\right\}^{-1}\left[-2\sigma\left\{\left(T^* + 1\right)m_e m_i^{-1} + 1\right\} + 2\alpha + m_i m_e^{-1}\left(T^* + \alpha\right)\right] + \left\{-k^{*^2} + \left(4R^2\right)^{-1}\right\}^{-2}\right.$$
$$\left.\left[-\sigma\left(1 + m_i m_e^{-1}\right) - 2\sigma m_e m_i^{-1} + \sigma^2 m_e m_i^{-1}\left(1 + m_e m_i^{-1}\right) + 2\sigma\right]\right] - 2^{-1}H_p^2 B_p\left(\Omega_{ge}^* M_{e\phi}^* + \Omega_{gi}^* M_{i\phi}^*\right)$$
$$\left. - 8M_\phi\omega_z^*\Omega_{ge}^* M_{e\phi} + \left(\Omega_{ge}^* M_{e\phi}^*\right)^2 + \left(4^{-1}H_p^2 B_p\right)^2 + 2\Omega_{gi}^* M_{i\phi}\left(-\Omega_{ge}^* M_{e\phi}^* + 2M_\phi\omega_z^*\right) + 12\left(M_\phi\omega_z^*\right)^2\right], \tag{6.42}$$

$$A_1 = -i\left\{ik^* + (2R)^{-1}\right\}^2\eta^*\left[\left[\left\{ik^* - (2R)^{-1}\right\}\left[\left(\Omega_{ge}^* M_{e\phi} - 4^{-1}H_p^2 B_p - 2M_\phi\omega_z^*\right)\left[2\sigma m_e m_i^{-1} - m_i m_e^{-1}\right.\right.\right.\right.$$
$$\left.\left.\left. - 2\alpha\left\{-k^{*^2} + \left(4R^2\right)^{-1}\right\}\right]\right] + \left\{-k^{*^2} + \left(4R^2\right)^{-1}\right\}\left[\Omega_{ge}^* M_{e\phi}\left(\Omega_{ge}^* M_{e\phi} - 2^{-1}H_p^2 B_p - 4M_\phi\omega_z^*\right)\right.$$
$$\left.\left.\left. + 4^{-1}H_p^2 B_p\left(4^{-1}H_p^2 B_p + 4M_\phi\omega_z^*\right) + 4\left(M_\phi\omega_z^*\right)^2\right]\right] + \left\{ik^* - (2R)^{-1}\right\}^2\left[-2\alpha\sigma m_e m_i^{-1} + \alpha m_i m_e^{-1}\right.$$
$$\left.\left. + \left\{-k^{*^2} + \left(4R^2\right)^{-1}\right\}^{-1}\left(\sigma m_e m_i^{-1} - m_i m_e^{-1}\right) + 2\alpha^2\left\{-k^{*^2} + \left(4R^2\right)^{-1}\right\}\right]\right], \tag{6.43}$$

$$A_0 = \left[-P + \left[\left\{k^{*^2} + \left(4R^2\right)^{-1}\right\}\left\{-k^{*^2} + \left(4R^2\right)^{-1}\right\}^{-1}m_i m_e^{-1}Q\right] + \left[2\left\{k^{*^2} + \left(4R^2\right)^{-1}\right\}^2\left\{-k^{*^2} + \left(4R^2\right)^{-1}\right\}^{-2}\sigma S\right]\right.$$
$$\left. - \left[\left\{k^{*^2} + \left(4R^2\right)^{-1}\right\}^3\left\{-k^{*^2} + \left(4R^2\right)^{-1}\right\}^{-2}\sigma^2\right] + \left[\left\{k^{*^2} + \left(4R^2\right)^{-1}\right\}\left\{-k^{*^2} + \left(4R^2\right)^{-1}\right\}^{-1}I\right]\right]. \tag{6.44}$$

The different terms substituted in A_0 are given in an expanded form as

$$
\begin{aligned}
P = &-\left\{ik^* + (2R)^{-1}\right\}^3\Big[\left\{ik^* - (2R)^{-1}\right\}\Big[\Big[2\alpha\Omega_{gi}^* M_{i\phi}\left(\Omega_{ge}^* M_{e\phi} - 2M_\phi\omega_z^*\right) - 4^{-1}H_p^2 B_p\left\{2\alpha\Omega_{gi}^* M_{i\phi} + 4\left(T^* + \alpha\right)M_\phi\omega_z^*\right\}\\
&- \Omega_{ge}^* M_{e\phi}T^*\left(\Omega_{ge}^* M_{e\phi} - 4M_\phi\omega_z^*\right) - 4^{-1}H_p^2 B_p T^*\left\{-2\Omega_{ge}^* M_{e\phi} + 4^{-1}H_p^2 B_p\right\} - 4M_\phi\omega_z^*\left\{T^* M_\phi\omega_z^*\right.\\
&\left. + \left(2M_\phi\omega_z^* - \Omega_{ge}^* M_{e\phi}\right)\alpha\right\}\Big] + \left\{-k^{*^2} + \left(4R^2\right)^{-1}\right\}^{-1}\Big[-2\Omega_{gi}^* M_{i\phi}\sigma m_e m_i^{-1}\left(\Omega_{ge}^* M_{e\phi} - 4^{-1}H_p^2 B_p - 4M_\phi\omega_z^*\right)\\
&- 4\sigma m_e m_i^{-1}M_\phi\omega_z^*\left(\Omega_{ge}^* M_{e\phi} - 4^{-1}H_p^2 B_p - 2M_\phi\omega_z^*\right) + \sigma 4^{-1}H_p^2 B_p\left(4^{-1}H_p^2 B_p + 4M_\phi\omega_z^*\right)\\
&- 2\Omega_{ge}^* M_{e\phi}\sigma\left\{2M_\phi\omega_z^*\left(1 - M_\phi\omega_z^*\right) + 4^{-1}H_p^2 B_p - 2^{-1}\Omega_{ge}^* M_{e\phi}\right\}\Big]\Big] + \left\{ik^* - (2R)^{-1}\right\}^2\Big[\Big[-\alpha\Big(\alpha\Omega_{gi}^* M_{i\phi}\\
&- 2\Omega_{ge}^* M_{e\phi}T^* + 2\alpha M_\phi\omega_z^*\Big) - 2\alpha T^*\left(2M_\phi\omega_z^* + 4^{-1}H_p^2 B_p\right)\Big] + \left\{-k^{*^2} + \left(4R^2\right)^{-1}\right\}^{-1}\Big[\sigma m_e m_i^{-1}\Big\{\Omega_{gi}^* M_{i\phi}\alpha\\
&+ T^*\left(2M_\phi\omega_z^* - \Omega_{ge}^* M_{e\phi}\right) + m_i m_e^{-1}\alpha 4^{-1}H_p^2 B_p\Big\} + \sigma m_e m_i^{-1}\Big\{2^{-1}H_p^2 B_p T + 4\alpha M_\phi\omega_z^* + 2m_i m_e^{-1}\left(2\alpha M_\phi\omega_z^*\right.\\
&\left.\left. - \Omega_{ge}^* M_{e\phi}\right)\Big\}\Big] + \left\{-k^{*^2} + \left(4R^2\right)^{-1}\right\}^{-2}\Big[-\sigma^2\left(m_e m_i^{-1}\right)^2\left(\Omega_{\mathrm{gi}}^* M_{i\phi} - 2m_i m_e^{-1}\Omega_{\mathrm{ge}}^* M_{e\phi} + 2M_\phi\omega_z^*\right) + \sigma^2 m_e m_i^{-1}\\
&\left(2^{-1}M_\phi\omega_z^* + \Omega_{ge}^* M_{e\phi} + 4^{-1}H_p^2 B_p\right)\Big]\Big] + \left\{ik^* - (2R)^{-1}\right\}^3\Big[-\alpha^2 T^* + \left\{-k^{*^2} + \left(4R^2\right)^{-1}\right\}^{-1}\left(2\alpha\sigma m_e m_i^{-1}T^* + \alpha^2\sigma^2\right)\\
&+ \left\{-k^{*^2} + \left(4R^2\right)^{-1}\right\}^{-2}\left\{-T^*\sigma^2\left(m_e m_i^{-1}\right)^2 - \alpha\sigma^2 m_e m_i^{-1}\right\}\Big] + \Omega_{\mathrm{gi}}^* M_{i\phi}\Omega_{\mathrm{ge}}^* M_{e\phi}\left(-\Omega_{\mathrm{ge}}^* M_{e\phi} + 4M_\phi\omega_z^*\right)\\
&+ 2^{-1}H_p^2 B_p\Omega_{\mathrm{gi}}^* M_{i\phi}\left(\Omega_{\mathrm{ge}}^* M_{e\phi} - 2M_\phi\omega_z^*\right) - \Omega_{\mathrm{gi}}^* M_{i\phi}\left(4^{-1}H_p^2 B_p\right)^2 - 4\left(M_\phi\omega_z^*\right)^2\left(\Omega_{\mathrm{gi}}^* M_{i\phi} - 2\Omega_{\mathrm{ge}}^* M_{e\phi} + 2M_\phi\omega_z^*\right)\\
&+ 2\Omega_{\mathrm{ge}}^* M_{e\phi}M_\phi\omega_z^*\left(-\Omega_{\mathrm{ge}}^* M_{e\phi} + 2^{-1}H_p^2 B_p\right) - M_\phi\omega_z^* 2^{-1}H_p^2 B_p\left(4^{-1}H_p^2 B_p + 4M_\phi\omega_z^*\right)\Big], \qquad (6.45)
\end{aligned}
$$

$$
\begin{aligned}
&\left[\left\{k^{*^2} + \left(4R^2\right)^{-1}\right\}\left\{-k^{*^2} + \left(4R^2\right)^{-1}\right\}^{-1} m_i m_e^{-1}Q\right]\\
&= -\left\{ik^* + (2R)^{-1}\right\}^3\Big[\left\{ik^* - (2R)^{-1}\right\}\left\{-k^{*^2} + \left(4R^2\right)^{-1}\right\}^{-1}\Big[m_i m_e^{-1}\Omega_{\mathrm{ge}}^* M_{e\phi}\left(\Omega_{\mathrm{gi}}^* M_{i\phi} + 2M_\phi\omega_z^*\right)\\
&- 4M_\phi\omega_z^* m_i m_e^{-1}\left(\Omega_{\mathrm{gi}}^* M_{i\phi} + M_\phi\omega_z^*\right) - m_i m_e^{-1}2^{-1}H_p^2 B_p M_\phi\omega_z^*\Big] + \left\{ik^* - (2R)^{-1}\right\}^2\Big[\left\{-k^{*^2} + \left(4R^2\right)^{-1}\right\}^{-1}\\
&\Big[m_i m_e^{-1}\left\{\Omega_{\mathrm{ge}}^* M_{e\phi} - \alpha\left(\Omega_{\mathrm{gi}}^* M_{i\phi} + 2M_\phi\omega_z^*\right)\right\} - m_i m_e^{-1}T^*\left(4^{-1}H_p^2 B_p + 2M_\phi\omega_z^*\right)\Big] + \left\{-k^{*^2} + \left(4R^2\right)^{-1}\right\}^{-2}\\
&\Big[-\sigma m_i m_e^{-1}\left(\Omega_{\mathrm{ge}}^* M_{e\phi} - 4^{-1}H_p^2 B_p - 2M_\phi\omega_z^*\right) + \sigma\left(\Omega_{\mathrm{gi}}^* M_{i\phi} + 2M_\phi\omega_z^*\right)\Big]\Big] + \left\{ik^* - (2R)^{-1}\right\}^3\Big[-\left\{-k^{*^2} + \left(4R^2\right)^{-1}\right\}^{-1}\\
&\alpha m_i m_e^{-1}T^* + \left\{-k^{*^2} + \left(4R^2\right)^{-1}\right\}^{-2}\sigma m_i m_e^{-1}\left(\alpha + m_e m_i^{-1}\right)\Big]\Big], \qquad (6.46)
\end{aligned}
$$

$$\left[2\left\{k^{*2}+\left(4R^2\right)^{-1}\right\}^2\left\{-k^{*2}+\left(4R^2\right)^{-1}\right\}^{-2}\sigma S\right]$$

$$=-2\sigma\left\{ik^*+(2R)^{-1}\right\}^3\left[-\left\{ik^*-(2R)^{-1}\right\}^2\left\{-k^{*2}+\left(4R^2\right)^{-1}\right\}^{-2}\left(\Omega_{\mathrm{ge}}^* M_{e\phi}-4^{-1}H_p^2B_p-2M_\phi\omega_z^*\right)\right.$$

$$\left.+\left\{ik^*-(2R)^{-1}\right\}^3\left\{-k^{*2}+\left(4R^2\right)^{-1}\right\}^{-2}\left[\alpha-\sigma\left\{-k^{*2}+\left(4R^2\right)^{-1}\right\}^{-1}m_e m_i^{-1}\right]\right], \tag{6.47}$$

$$\left[\left\{k^{*2}+\left(4R^2\right)^{-1}\right\}\left\{-k^{*2}+\left(4R^2\right)^{-1}\right\}^{-1}I\right]$$

$$=-\left\{ik^*+(2R)^{-1}\right\}^3\left[\left\{ik^*-(2R)^{-1}\right\}\left\{-k^{*2}+\left(4R^2\right)^{-1}\right\}^{-1}\left[\Omega_{\mathrm{ge}}^* M_{e\phi}\left(-\Omega_{\mathrm{ge}}^* M_{e\phi}+2^{-1}H_p^2B_p+4M_\phi\omega_z^*\right)\right.\right.$$

$$\left.-4^{-1}H_p^2B_p\left(4^{-1}H_p^2B_p+4M_\phi\omega_z^*\right)-4\left(M_\phi\omega_z^*\right)^2\right]+\left\{ik^*-(2R)^{-1}\right\}^2\left[-\left\{-k^{*2}+\left(4R^2\right)^{-1}\right\}^{-1}\left(-\Omega_{\mathrm{ge}}^* M_{e\phi}\right.\right.$$

$$\left.\left.+4^{-1}H_p^2B_p+2M_\phi\omega_z^*\right)+\left\{-k^{*2}+\left(4R^2\right)^{-1}\right\}^{-2}\left\{-2\sigma m_e m_i^{-1}\left(2\Omega_{\mathrm{ge}}^* M_{e\phi}-4^{-1}H_p^2B_p-2M_\phi\omega_z^*\right)\right\}\right]$$

$$\left.+\left\{ik^*-(2R)^{-1}\right\}^3\left[-\left\{-k^{*2}+\left(4R^2\right)^{-1}\right\}^{-1}\alpha^2+\left\{-k^{*2}+\left(4R^2\right)^{-1}\right\}^{-2}\left(2\alpha\sigma m_e m_i^{-1}\right)-\left\{-k^{*2}+\left(4R^2\right)^{-1}\right\}^{-3}\left(\sigma m_e m_i^{-1}\right)^2\right]\right]. \tag{6.48}$$

The sextic dispersion relation (equation (6.38)) is transformed into a reduced form in light of the low-frequency approximation with the help of traditional simplification procedure [34]. We are primarily interested in the low-frequency limit because we wish to investigate the cylindrical acoustic waves. In the low-frequency limit $\left(\Omega^q=0,\forall\, q>1\right)$, the modified dispersion relation is cast as

$$A_1\Omega+A_0=0\,. \tag{6.49}$$

The coefficients A_1 - A_0 are given in equations (6.43)-(6.44), respectively. We then analyze the dispersion relation in four distinct regimes of our interest, namely in quantum (completely degenerate) non-planar (cylindrical), quantum (completely degenerate) planar, classical (completely non-degenerate) non-planar (cylindrical), classical (completely non-degenerate) planar.

6.3.1 Quantum (completely degenerate) non-planar regime

In the quantum non-planar regime, we have the same dispersion relation as given by equation (6.49). Likewise, the coefficients are the same as given by equations (6.43) and (6.44). α for the completely degenerate case is substituted from equation (6.35).

6.3.2 Quantum (completely degenerate) planar regime

In the quantum planar regime, we have $R \to \infty$. The dispersion relation is the same as equation (6.49). However, the coefficients given by equations (6.43) and (6.44) are modified. α for the completely degenerate case is substituted from equation (6.35). The cylindrical coordinates are mapped into planar coordinates accordingly. The modified coefficients are given as

$$A_1 = ik^{*2}\eta^* \left[\left[\left(ik^*\right)\left[\left(\Omega_{ge}^* M_{ey} - 4^{-1}H_p^2 B_p - 2M_y\omega_z^*\right)\left[2\sigma m_e m_i^{-1} - m_i m_e^{-1} + 2\alpha k^{*2}\right]\right]\right.\right.$$
$$- k^{*2}\left[\Omega_{ge}^* M_{ey}\left(\Omega_{ge}^* M_{ey} - 2^{-1}H_p^2 B_p - 4M_y\omega_z^*\right) + 4^{-1}H_p^2 B_p\left(4^{-1}H_p^2 B_p + 4M_y\omega_z^*\right) + 4\left(M_y\omega_z^*\right)^2\right]\left.\right]$$
$$\left. - k^{*2}\left[-2\alpha\sigma m_e m_i^{-1} + \alpha m_i m_e^{-1} - k^{*2}\left(\sigma m_e m_i^{-1} - m_i m_e^{-1}\right) - 2\alpha^2 k^{*2}\right]\right], \qquad (6.50)$$

$$A_0 = \left[-P - \left(m_i m_e^{-1}Q\right) - \left(2\sigma S\right) - k^{*2}\sigma^2 - I\right]. \qquad (6.51)$$

The different substituted terms in equation (6.51) are modified accordingly.

6.3.3 Classical (completely non-degenerate) non-planar regime

In the classical non-planar regime, the Bohm potential term is ignored. The dispersion relation is the same as equation (6.49), however, the coefficients A_1 and A_0 are modified. α for the classical case is substituted from equation (6.36). The coefficients are modified as

$$A_1 = -i\left\{ik^* + (2R)^{-1}\right\}^2\eta^*\left[\left[\left\{ik^* - (2R)^{-1}\right\}\left[\left(\Omega_{ge}^* M_{e\phi} - 2M_\phi\omega_z^*\right)\left[2\sigma m_e m_i^{-1} - m_i m_e^{-1} - 2\alpha\left\{-k^{*2} + \left(4R^2\right)^{-1}\right\}\right]\right]\right.\right.$$
$$\left. + \left\{-k^{*2} + \left(4R^2\right)^{-1}\right\}\left[\Omega_{ge}^* M_{e\phi}\left(\Omega_{ge}^* M_{e\phi} - 4M_\phi\omega_z^*\right) + 4\left(M_\phi\omega_z^*\right)^2\right]\right] + \left\{ik^* - (2R)^{-1}\right\}^2\left[-2\alpha\sigma m_e m_i^{-1} + \alpha m_i m_e^{-1}\right.$$
$$\left.\left. + \left\{-k^{*2} + \left(4R^2\right)^{-1}\right\}^{-1}\left(\sigma m_e m_i^{-1} - m_i m_e^{-1}\right) + 2\alpha^2\left\{-k^{*2} + \left(4R^2\right)^{-1}\right\}\right]\right], \qquad (6.52)$$

$$A_0 = \left[-P + \left[\left\{ k^{*2} + \left(4R^2\right)^{-1} \right\} \left\{ -k^{*2} + \left(4R^2\right)^{-1} \right\}^{-1} m_i m_e^{-1} Q \right] + \left[2 \left\{ k^{*2} + \left(4R^2\right)^{-1} \right\}^2 \left\{ -k^{*2} + \left(4R^2\right)^{-1} \right\}^{-2} \sigma S \right] \right.$$
$$\left. - \left[\left\{ k^{*2} + \left(4R^2\right)^{-1} \right\}^3 \left\{ -k^{*2} + \left(4R^2\right)^{-1} \right\}^{-2} \sigma^2 \right] + \left[\left\{ k^{*2} + \left(4R^2\right)^{-1} \right\} \left\{ -k^{*2} + \left(4R^2\right)^{-1} \right\}^{-1} I \right] \right] . \qquad (6.53)$$

The different substituted terms appearing in equation (6.53) are modified as per the approximations stated in section 6.3.3.

6.3.4 Classical (completely non-degenerate) planar regime

In the classical (completely non-degenerate) planar regime, we have $R \to \infty$. Just like the classical non-planar regime, Bohm potential is also ignored herein. The dispersion relation is the same as given by equation (6.49). The coefficients appearing in equation (6.49) are modified as per the considered regime. The cylindrical coordinates are conveniently mapped into planar coordinates. α for the classical case is substituted from equation (6.36). The modified coefficients A_1 and A_0 are given as

$$A_1 = ik^{*2}\eta^* \left[\left[\left(ik^*\right) \left(\Omega_{ge}^* M_{ey} - 2M_y \omega_z^* \right) \left[2\sigma m_e m_i^{-1} - m_i m_e^{-1} + 2\alpha k^{*2} \right] \right] \right.$$
$$- k^{*2} \left[\Omega_{ge}^* M_{ey} \left(\Omega_{ge}^* M_{ey} - 4M_y \omega_z^* \right) + 4\left(M_y \omega_z^*\right)^2 \right] \Big]$$
$$\left. - k^{*2} \left[-2\alpha\sigma m_e m_i^{-1} + \alpha m_i m_e^{-1} - k^{*-2} \left(\sigma m_e m_i^{-1} - m_i m_e^{-1} \right) - 2\alpha^2 k^{*2} \right] \right], \qquad (6.54)$$

$$A_0 = \left[-P - \left(m_i m_e^{-1} Q\right) - \left(2\sigma S\right) - k^{*2}\sigma^2 - I \right]. \qquad (6.55)$$

The different terms appearing in equation (6.55) are modified as per our approximations (as in section 6.4.4).

The above discussion in the subsections are summarily pointed out as

- In the quantum non-planar regime, the dispersion relation has the contribution due to the geometric curvature effect, Lorentz force, Coriolis rotational force, kinematic viscosity, quantum parameter, Bohm potential, quantum pressure, temperature, and Jeans-to-plasma oscillation frequency ratio squared. The growth patterns for different parameters are depicted in figures 6.1-6.5.

- In the quantum planar regime, the reduced dispersion relation has the dependencies of all the above terms except the geometric curvature. The growth/damping trends of the same for different relevant parameters are given in figures 6.6-6.10.
- For the classical non-planar regime, the dispersion relation has the dependencies of all the terms as the quantum non-planar regime, except the Bohm potential term. The quantum pressure also gets replaced with the classical pressure. The growth/damp trends for the same are given in figures 6.11-6.15.
- Lastly, for the classical planar regime, the dispersion relation highlights the contribution of all the terms as the classical non-planar regime, except the geometric curvature terms. The growth/damp trends for the relevant parameters in this regime are graphically seen in figures 6.16-6.20.

Thus, it is clearly seen that, in all the four considered distinct regimes, the modified dispersion relation has sensitive dependencies on the multiparametric model coefficients influencing the stability dynamics of the considered plasma system.

6.4 RESULTS AND DISCUSSIONS

The excitation and stability features of cylindrical acoustic waves are analyzed by means of a two-component axisymmetric magnetized cylindrical plasma system comprising of electrons and ions. The system is rotating uniformly with its angular velocity directed longitudinally. The electrons evolve under the action of their motion, electrostatic potential, Lorentz force, Coriolis rotational force, Bohm potential and gravitational potential. Meanwhile the ionic dynamics is governed by all of the above mentioned factors, except the Bohm potential term. In addition, kinematic viscosity is retained for the ionic dynamics. The temperature degeneracy of electrons is incorporated via the temperature degeneracy parameter in the equation of state for the electrons. The ions experience the normal classical thermal pressure. A standard cylindrical mode analysis employing the Hankel function yields a generalized linear sextic dispersion relation, which is modified using the low-frequency approximation [24]. A numerical illustrative platform is used to analyze the growth rate corresponding to the acoustic excitation and stability in four parametric windows, namely the quantum non-planar, quantum planar, classical non-planar, and classical planar. Here, the dispersion analysis of current interest in different regimes is systematically carried out

by analyzing equation (6.49) graphically, as clearly depicted in figures 6.1-6.20. It is noteworthy that different input values used herein exist in the literature [35-42]. There are certain debates regarding the input values and their validity in the classical and quantum domains [43-45]. The number density and temperature range for the quantum regime are given [43] as 10^{24}-10^{30} cm^{-3} and 10^{2}-10^{7} K, respectively. In SI units, the number density is 10^{30}-10^{36} m^{-3}. This is in agreement with the values considered for the quantum regime in the manuscript. Likewise, for the classical regime, the number density and temperature range are given [43] as 10^{6}-10^{24} cm^{-3} and 10^{4}-10^{7} K. In SI units, the number density is 10^{12}-10^{30} m^{-3}. The values for the classical regime in the manuscript are also in good agreement with the specified values of the previous study [43]. Apart from a common feature of extreme growth of the fluctuations at extremely large wavelengths, the uncommon features of the same are described and interpreted in the following subsections.

6.4.1 Quantum (completely degenerate) non-planar regime

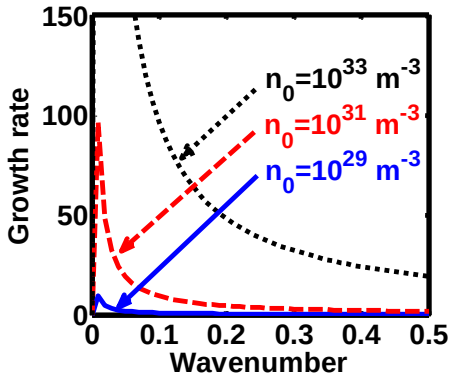

Figure 6.1*: Profile of the normalized growth rate* (Ω_i) *with variation in the normalized wavenumber* (k^*)*. The different lines link to different values of the equilibrium number density* (n_0) *in non-planar (cylindrical) geometry in the quantum regime.*

In figure 6.1, we depict the profile structures of the normalized growth rate (Ω_i) with variation in the normalized wavenumber (k^*), which results numerically from equation (6.49), for different values of the equilibrium number density (n_0). The different coloured lines link to $n_0 = 10^{29}$ m^{-3} (blue solid line), $n_0 = 10^{31}$ m^{-3} (red dashed

line), and $n_0 = 10^{33}$ m^{-3} (black dotted line). As clearly evident from figure 6.1, the growth rate increases with increasing number density. The physical reason behind this can be ascribed to the fact that higher the mass of the system, higher is the possibility of exciting gravitational instability [46]. It couples with the background fluctuations resulting in the growth.

In figure 6.2, we depict the same as figure 6.1, but for different indicated values of the normalized kinematic viscosity (η^*). The corresponding unnormalized viscosity values (η) are alongside highlighted for the sake of our easy understanding. The different coloured lines link to $\eta = 10^{-3}$ kg m^{-1} s^{-1} ($\eta^* = 24.91\times10^{-6}$, blue solid line), $\eta = 10^{-2}$ kg m^{-1} s^{-1} ($\eta^* = 24.91\times10^{-7}$, red dashed line), $\eta = 10^{-1}$ kg m^{-1} s^{-1} ($\eta^* = 2.49\times10^{-3}$, black dotted line). The trends shown by the different coloured lines indicate that an increase in the viscosity gradually decreases the instability growth rate, thereby exhibiting stabilizing influence on the system. This can be physically attributed to the fact that with an increase in the viscosity, the cohesion among fluid layers increases [37]. It means that the interspecies force gets enhanced; thereby, restricting the relative fluid motion. The fluid viscosity here plays a stabilization role against the perturbation dynamics under the current exploration.

In figure 6.3, we indicate the same as figure 6.1, but for different values of the normalized Coriolis rotational force (C_F^*). The different coloured lines link to $C_F^* = 0.008$ (blue solid line), $C_F^* = 0.01$ (red dashed line), and $C_F^* = 0.012$ (black dotted line). We see that the system has significant growth only in the long-wavelength regime ($k^* \to 0$). It is indicated that higher the Coriolis rotational force, higher is the destabilization of the system; and vice-versa. It can be physically attributed to the fact that, higher the Coriolis rotation of the system, higher is the rotational kinetic energy, $E_r = (1/2)I\omega_r^2 = (1/2)MK_g^2\omega_r^2$, and vice-versa. Here, I is the system moment of inertia around the reference axis of rotation, M is the inertial mass of the system with angular velocity ω_r and K_g is its radius of gyration around the same rotation axis. We assume a uniform rotation of the system, which, thereby implicates that $E_r \propto M$. It is a well-established fact that heavier objects are gravitationally unstable as compared to their lighter counterparts. Thus, an increase in the Coriolis rotation destabilizes the system,

and vice-versa. It is in accordance with the previous results by us [20] and astronomical evidences observed by others [47, 48].

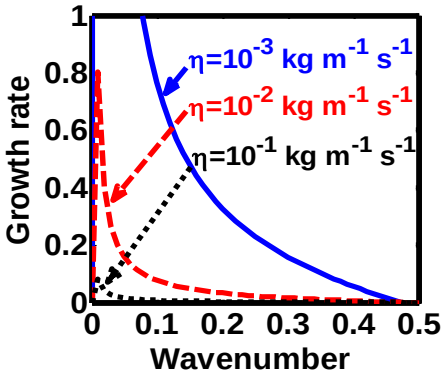

Figure 6.2: *Same as figure 6.1, but for different values of the normalized kinematic viscosity* (η^*).

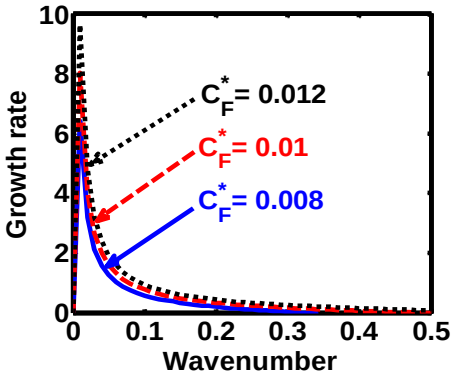

Figure 6.3: *Same as figure 6.1, but for different values of the normalized Coriolis rotational force* (C_F^*).

As in figure 6.4, we depict the same as figure 6.1, but for different indicated values of the normalized thermal temperature (T^*). Here, just like figure 6.2, the unnormalized values of the temperature are indicated in figure 6.4. The different coloured lines link to $T = 10^3$ K ($T^* = 8.26\times10^{-8}$, blue solid line), $T = 10^4$ K ($T^* = 8.26\times10^{-7}$, red dashed line), and $T = 10^5$ K ($T^* = 8.26\times10^{-6}$, black dotted line). The different coloured lines clearly indicate that, an increase in the temperature destabilizes the system, and vice-versa. It is indeed a well-established fact that a temperature increase enhances the system kinetic energy, and so on. It, hereby,

randomizes the system at the cost of enhanced particle thermal motion resulting in destabilization of the system. In other words, it is noteworthy that microscopic thermal motions of the individual constitutive particles significantly contribute to the bulk development of an anti-centric thermal pressure force (outward, randomizing) against the concentric gravitational counterpart (inward, organizing), causing the bulk destabilization consequences.

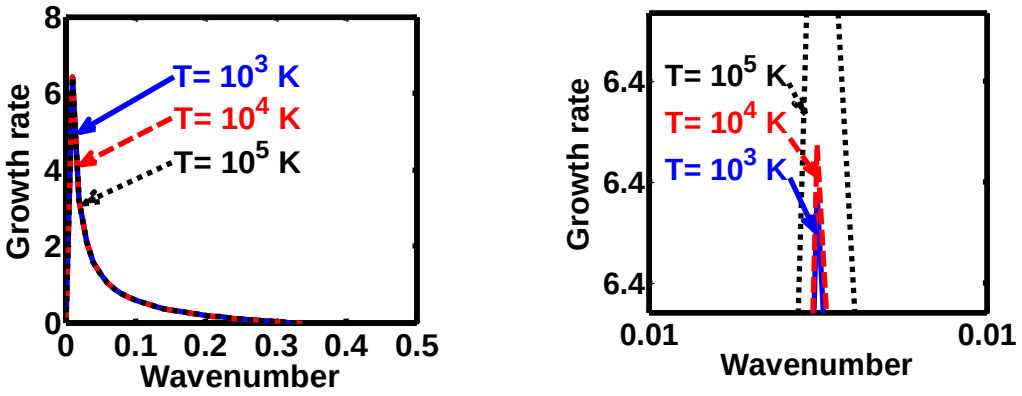

Figure 6.4: *Same as figure 6.1, but for different values of the normalized thermal temperature* (T^*). *The second subplot is the magnified version depicting the peaks (kinks) clearly.*

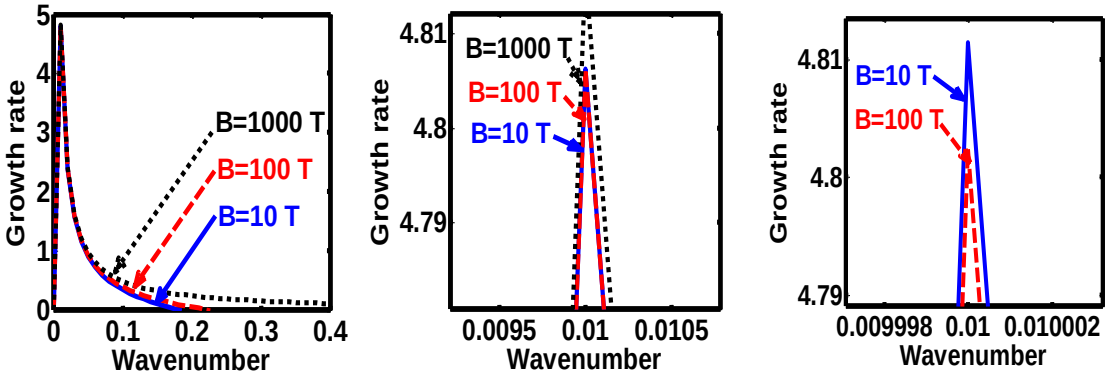

Figure 6.5: *Same as figure 6.1, but for different values of magnetic field* (B). *The two subsequent subplots depict the magnified versions clearly highlighting the peaks (kinks).*

In a similar way, figure 6.5 shows the same as figure 6.1, but for different values of the magnetic field. The different coloured lines correspond to $B = 10$ T (blue solid line), $B = 100$ T (red dashed line), and $B = 1000$ T (black dotted line). An interesting

hybrid trend of growth peaks in different magnetic conditions is found to exist. It is against the previous cases showing a definite multiparametric increasing or decreasing growth pattern (figures 6.1-6.4). In other words, figure 6.5 shows a unique admixture of fluctuation growth patterns. Here, the growth rate is highest for $B = 1000$ T, followed by the subsequent gradually weaker growths produced at $B = 10$ T and $B = 100$ T, respectively. The non-uniformity in the instability growth-peak order with the magnetic field strength found here is a new and unique behaviour exhibited by this categorical class of collective fluctuation dynamics.

6.4.2 Quantum (completely degenerate) planar regime

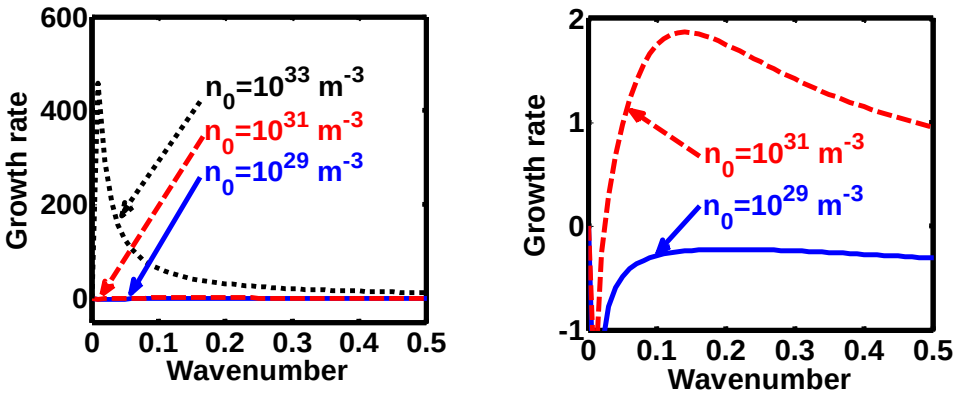

Figure 6.6: *Profile of the normalized growth rate* (Ω_i) *with variation in the normalized wavenumber* (k^*)*. The different lines link to different values of the equilibrium number density* (n_0) *in planar (non-cylindrical) geometry in the quantum regime. The second subplot is the enlarged version highlighting the trends for* $n_0 = 10^{29}$ m^{-3} *and* $n_0 = 10^{31}$ m^{-3}.

In figure 6.6, we depict the same as figure 6.1, but for the quantum planar geometric regime. The colour spectral coding is the same as that of figure 6.1. Clearly, the growth rate increases with increasing number density, and vice-versa. This is physically due to the well-established fact that heavier objects are gravitationally more unstable as compared to their lighter counterparts on the astrophysical scales. Even though the trend shown by figure 6.1 (quantum non-planar regime) is the same as figure 6.6 (quantum planar regime), the growth rate of the considered fluctuation dynamics is considerably higher for the latter.

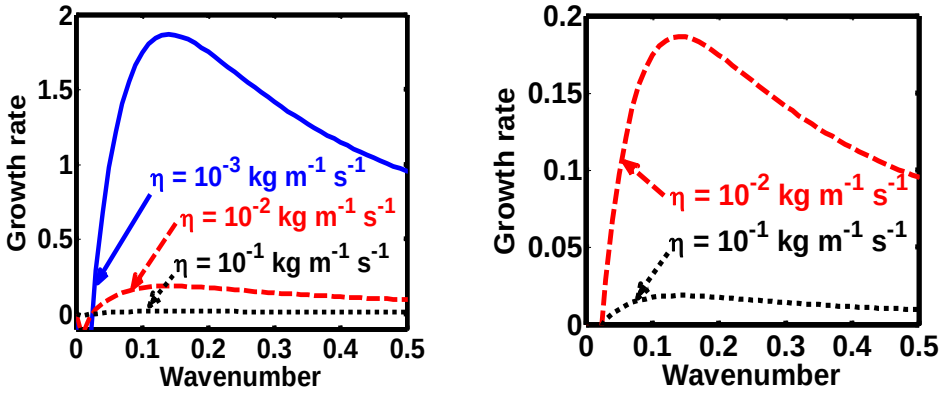

Figure 6.7: *Same as figure 6.6, but for different values of the normalized kinematic viscosity* (η^*). *The second subplot is the enlarged version clearly highlighting the trends for* $\eta = 10^{-2}$ *kg m*$^{-1}$ *s*$^{-1}$ *and* $\eta = 10^{-1}$ *kg m*$^{-1}$ *s*$^{-1}$.

In an analogous way, figure 6.7 shows the same as figure 6.2, but for the quantum planar regime. The colours used here are the same as that of figure 6.2. Clearly, the growth rate decreases with increase in the kinematic viscosity, and vice-versa. It may, therefore, be inferred that viscosity enhancement leads to the stabilization of the self-gravitating system, and vice-versa. The physical reason behind this is the same as described in figure 6.2. Viscosity playing as a stabilizing role in self-gravitating systems is a well-known fact established in the literature [37].

Similarly, figure 6.8 shows the same as figure 6.3, but for the quantum planar regime. As can be clearly seen herefrom, the growth rate of the system increases with an increase in strength of the Coriolis rotational force. The physical reason behind this behaviour is the same as that of figure 6.3.

Figure 6.9 depicts the same as figure 6.4, but for the quantum planar regime. An enhancement in the temperature increases the kinetic energy of the constitutive particles, thereby increasing the disturbance in the system. As a result, the instability growth rate of the considered instability increases with the temperature, and vice-versa.

Figure 6.10 shows the same as figure 6.5, but for the quantum planar regime. The colour spectral coding used here is exactly the same as that used in figure 6.5. An absurd behaviour is seen to exist in the case of the magnetic field enhancement followed by a simultaneous existence of both growth dips and peaks. More specifically, while $B = 10$ T and $B = 100$ T give growth dips; in contrast, $B = 1000$ T results in growth peak, and so forth.

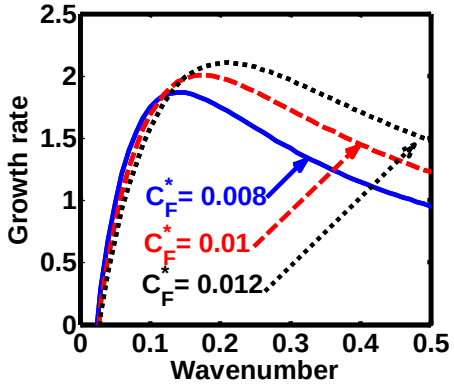

Figure 6.8: *Same as figure 6.6, but for different values of the normalized Coriolis rotational force* $\left(C_F^*\right)$.

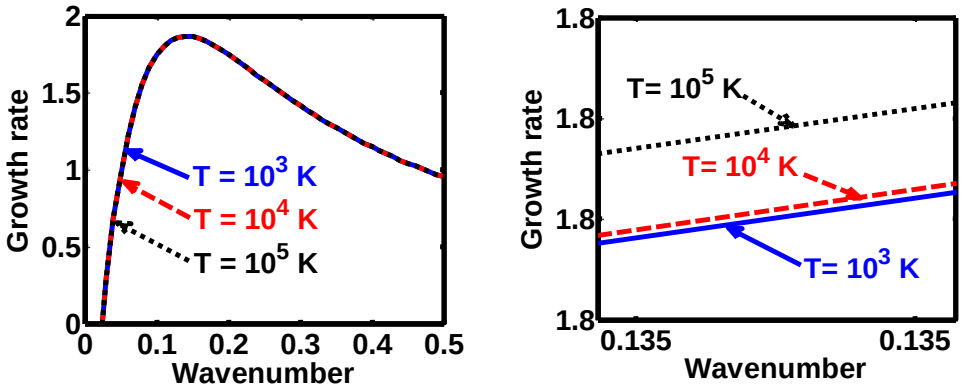

Figure 6.9: *Same as figure 6.6, but for different values of the normalized thermal temperature* $\left(T^*\right)$. *The second subplot is the magnified version depicting the peaks clearly.*

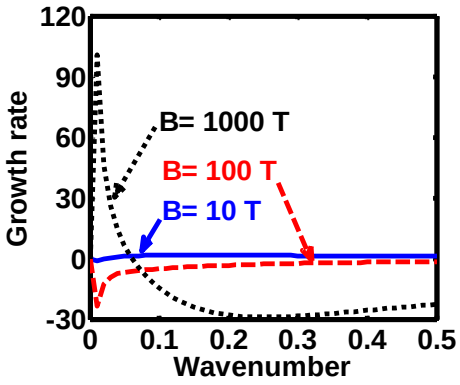

Figure 6.10: *Same as figure 6.6, but for different values of the magnetic field* $\left(B\right)$.

6.4.3 Classical (completely non-degenerate) non-planar regime

In figure 6.11, we depict the profile structures of the normalized growth rate (Ω_i) with variation in the normalized wavenumber (k^*) for different values of the equilibrium number density (n_0). The different coloured lines link to $n_0 = 10^{21}$ m^{-3} (blue solid line), $n_0 = 10^{23}$m^{-3} (red dashed line), and $n_0 = 10^{25}$ m^{-3} (black dotted line). It is found that an enhancement in the equilibrium number density increases the growth rate, and vice-versa. This growth behaviour is the same as that observed in both the quantum regimes discussed previously (figures 6.1, 6.6). The physical insight behind such instability growth features is the same as that already described in figure 6.1.

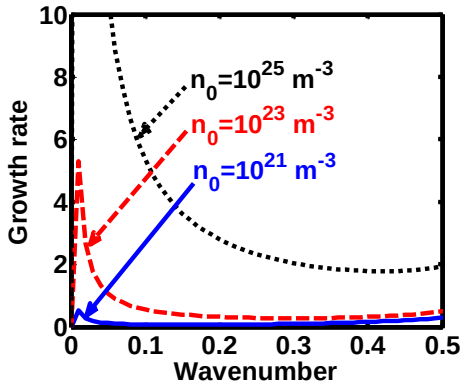

Figure 6.11: *Profile of the normalized growth rate* (Ω_i) *with variation in the normalized wavenumber* (k^*). *The different lines link to different values of the equilibrium number density* (n_0) *in non-planar (cylindrical) geometry in the classical regime.*

Figure 6.12 shows the same as figure 6.11, but for different values of the normalized kinematic viscosity (η^*). Here, the unnormalized (normalized) values of the kinematic viscosity are indicated for our easy comprehension. The different coloured lines link to $\eta = 10^{-3}$ kg m^{-1} s^{-1} ($\eta^* = 3.03\times10^4$, blue solid line), $\eta = 10^{-2}$ kg m^{-1} s^{-1} ($\eta^* = 3.03\times10^5$, red dashed line), $\eta = 10^{-1}$ kg m^{-1} s^{-1} ($\eta^* = 3.03\times10^6$, black dotted line). An enhancement in the value of kinematic viscosity again stabilizes the system. The physical reason behind this trend is the same as in figure 6.2.

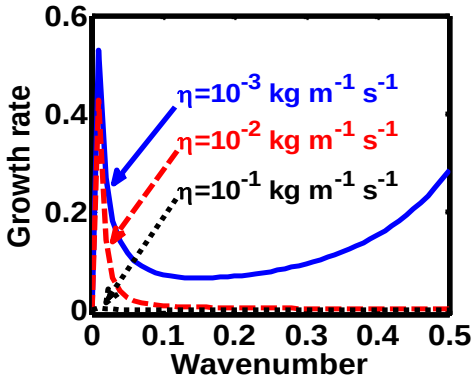

Figure 6.12: *Same as figure 6.11, but for different values of the normalized kinematic viscosity* (η^*).

Figure 6.13 shows the same as figure 6.11, but for different values of the Coriolis rotational force (C_F^*). The different coloured lines correspond to $C_F^* = 0.008$ (blue solid line), $C_F^* = 0.01$ (red dashed line), and $C_F^* = 0.012$ (black dotted line). It clearly indicates that the Coriolis force enhancement destabilizes the system, and vice-versa. The physical reason is the same as figure 6.3.

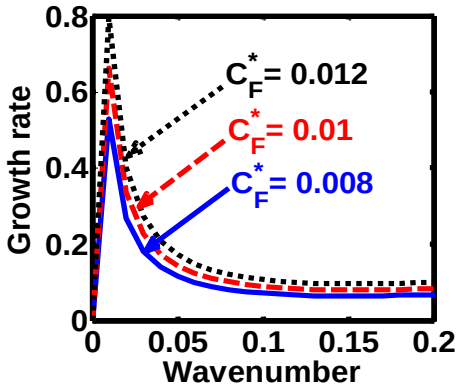

Figure 6.13: *Same as figure 6.11, but for different values of the normalized Coriolis rotational force* (C_F^*).

Figure 6.14 shows the same as figure 6.11, but for different values of the normalized thermal temperature. The different coloured lines link to $T = 10^5$ K ($T = 1.84 \times 10^3$, blue solid line), $T = 10^6$ K ($T = 1.84 \times 10^4$, red dashed line), and $T = 10^7$ K ($T = 1.84 \times 10^5$, black dotted line). It can be clearly seen that the growth rate of the system increases with an increase in the temperature in the considered configuration, and so

forth. It hereby implies that the temperature acts as a destabilization agent under the joint action of all the considered factors.

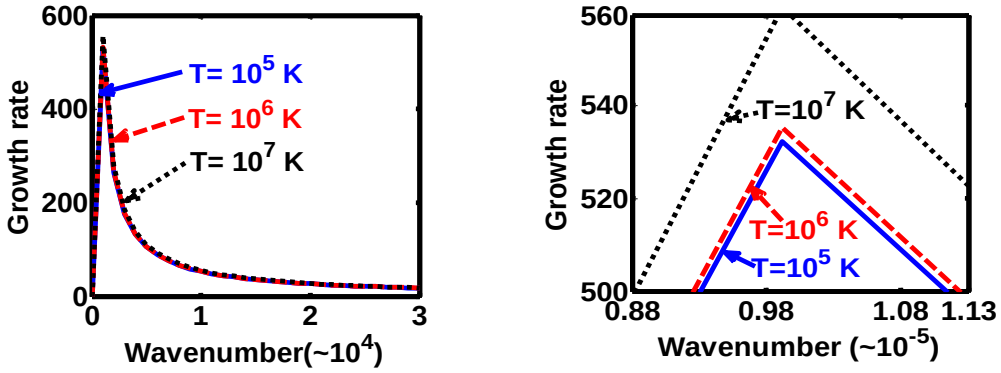

Figure 6.14: *Same as figure 6.11, but for different values of the normalized thermal temperature* (T^*). *The second subplot is the magnified version depicting the peaks (kinks) clearly.*

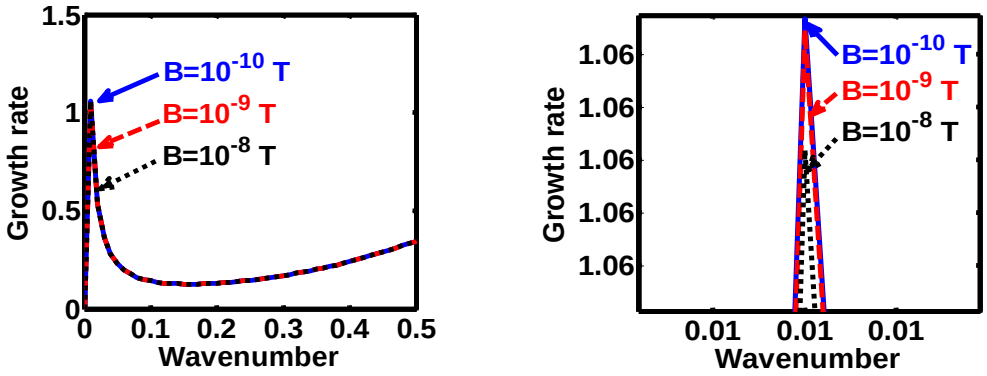

Figure 6.15: *Same as figure 6.11, but for different values of the magnetic field* (B). *The second subplot is the magnified version depicting the peaks (kinks) clearly.*

Figure 6.15 shows the same as figure 6.11, but for different values of the magnetic field. The different coloured lines correspond to $B=10^{-10}$ T (blue solid line), $B=10^{-9}$ T (red dashed line), and $B=10^{-8}$ T (black dotted line). In contrast to the hybrid behaviour displayed in both the quantum regimes, the magnetic field, in case of classical non-planar regime, shows a definite trend. The growth rate of the instability decreases on increasing the magnetic field, and vice-versa. It is founded on the basics of plasma confinement processes in an external magnetic field. Due to an increase in

plasma confinement on the magnetic field enhancement, the instability growth rate of the system decreases, and vice-versa. The same has also been pointed out in the previous investigations reported in the literature elsewhere [20].

6.4.4 Classical (completely non-degenerate) planar regime

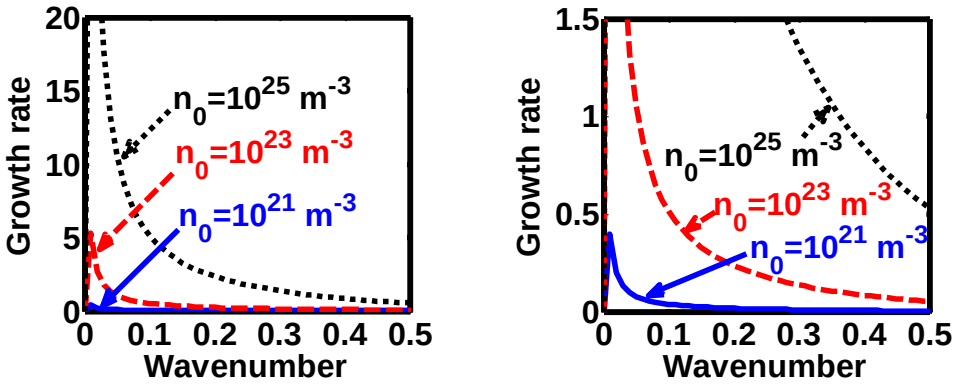

Figure 6.16: *Profile of the normalized growth rate* (Ω_i) *with variation in the normalized wavenumber* (k^*). *The different lines link to different values of the equilibrium number density* (n_0) *in planar (non-cylindrical) geometry in the classical regime. The second subplot is its enlarged version clearly showing the trends for* $n_0 = 10^{21}\ m^{-3}$ *and* $n_0 = 10^{23}\ m^{-3}$.

In the classical (completely non-degenerate) regime, figure 6.16 shows the same as figure 6.11, but for the plane geometry approximation. It can be clearly seen herein that the growth rate increases with the equilibrium number density, and vice-versa. The explanation behind the observed trend is the same as figure 6.1.

Again, figure 6.17 shows the same as figure 6.12, but for the classical planar regime. As clearly evident herein, the growth rate decreases with increase in the kinematic viscosity value, and vice-versa. The explanation behind this growth trend is already presented in case of figure 6.2.

Furthermore, figure 6.18 shows the same as figure 6.13, but for the classical plane-geometry regime. It can be clearly inferred from here that the growth rate increases with the strength of the Coriolis rotational force, and vice-versa. The physical mechanism operating behind this growth pattern trend is the same as figure 6.3; and so forth.

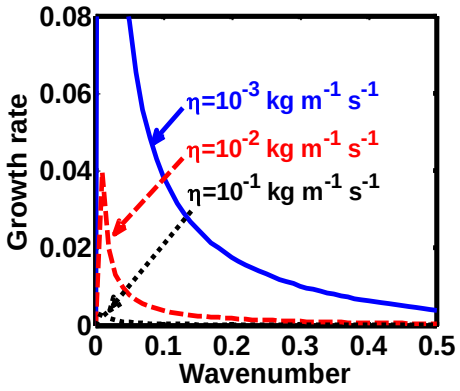

Figure 6.17: *Same as figure 6.16, but for different values of the normalized kinematic viscosity* (η^*).

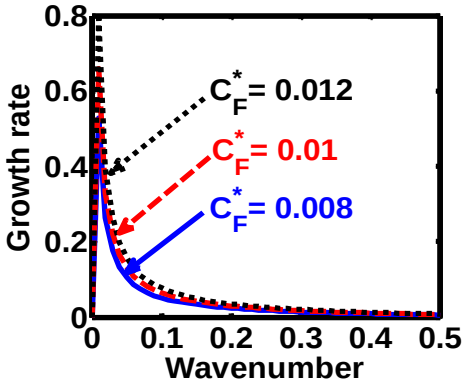

Figure 6.18: *Same as figure 6.16, but for different values of the normalized Coriolis rotational force* (C_F^*).

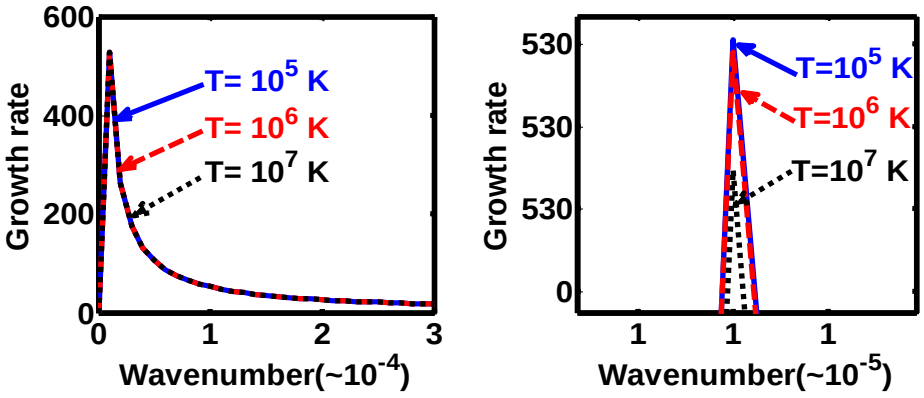

Figure 6.19: *Same as figure 6.16, but for different values of the normalized thermal temperature* (T^*). *The second subplot is the magnified version depicting the peaks (kinks) clearly.*

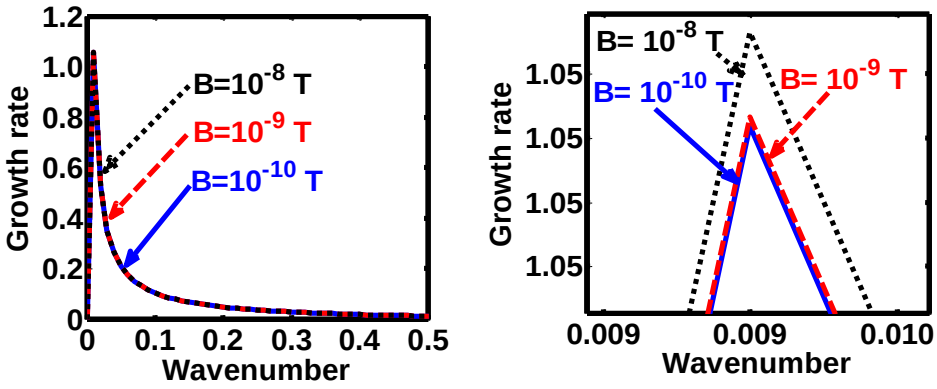

Figure 6.20: *Same as figure 6.16, but for different values of the magnetic field* (B). *The second subplot is the magnified version depicting the peaks (kinks) clearly.*

Likewise, figure 6.19 shows the same as figure 6.14, but for the classical planar regime. Interestingly, figure 6.19 shows an opposite growth trend against figure 6.14. In other words, in figure 6.19, a temperature enhancement stabilizes the system, and vice-versa. That is, the growth rate of the system decreases with increase in the temperature, and vice-versa. It is a well-known fact that an increase in the temperature increases the kinetic energy of the system, and so forth. Thus, an excessive kinetic energy gained on a high temperature scale is dissipated away to the surroundings, thus reducing the kinetic energy of the system. As a consequence, higher the temperature, higher is the kinetic energy, and higher will be the rate of dissipation, thereby decreasing the instability growth rate.

At the last, figure 6.20 shows the same as figure 6.15, but for the classical planar regime. Interestingly, an opposite behavioural pattern of the instability growth is observed herein against figure 6.15. That is, the growth rate of the instability increases with the strength of the magnetic field, and vice-versa. This is because, for the plasma to be confined in a magnetic field, a certain curvature drift effect is required, which is, however, missing in the case of the classical planar regime [49]. Moreover, enhanced magnetic field strength increases the gyrofrequency of the constitutive particles. It hereby leads to the system destabilization on the Larmor kinetic footing. To sum up, a compact table highlighting a brief contrast on the fluctuation dynamics in the four distinct regimes for the sake of readers is given.

Table 6.1: A relative contrast of fluctuation dynamics

S. No.	Parameter	Quantum non-planar	Quantum planar	Classical non-planar	Classical planar
1.	Equilibrium number density	Destabilizer	Destabilizer	Destabilizer	Destabilizer
2.	Kinematic viscosity	Stabilizer	Stabilizer	Stabilizer	Stabilizer
3.	Coriolis rotation	Destabilizer	Destabilizer	Destabilizer	Destabilizer
4.	Temperature	Destabilizer	Destabilizer	Destabilizer	Stabilizer
5.	Magnetic field	Mixed role	Absurd	Stabilizer	Destabilizer

On the basis of the above described results, it can clearly be inferred that, in the quantum regime, the equilibrium number density plays the most dominant role in destabilizing the system. However, in the classical regime, the system temperature plays a major role in stabilizing/destabilizing the system. Moreover, the destabilizing nature of rotational force is observationally accounted in many white dwarf stars [47] and circumstellar discs [48].

6.5 CONCLUSIONS

In our proposed semi-analytic study, a two-component quantum hydrodynamic plasma model is presented to analyze the excitation and stability dynamics of cylindrical acoustic waves excitable in gyrogravitating magnetized cylindrical astrophysical structures. The electronic dynamics is subject to the conjoint action of electrostatic potential, Lorentz force, Coriolis rotational force, Bohm potential, and temperature degeneracy effects. The temperature degeneracy parameter in the electronic equation of state results in a completely degenerate quantum (Fermi) pressure and a completely non-degenerate classical (thermal) pressure in judicious approximations in correlation with realistic scenarios. The constitutive classical ionic fluid dynamics is modelled jointly with the electrostatic potential, Lorentz force, Coriolis rotational force, and kinematic viscosity. Thus, the electronic fluid is affected by the quantum potential; whereas, it is only the ionic fluid that is affected by the kinematic viscosity classically. Accordingly, the constitutive ions are acted upon by the classical thermal pressure. A cylindrical normal mode analysis, employing the Hankel function formalism, yields a

generalized linear sextic dispersion relation. The low-frequency acoustic regime is then thoroughly investigated in four distinct parametric regimes of practical importance. It includes the quantum non-planar, quantum planar, classical non-planar, and classical planar windows. The obtained results on the diverse stability factors in an itemized form are summarily presented as follows.

1) *Quantum non-planar regime*: In this regime, the equilibrium number density, Coriolis force, and temperature destabilize the plasma system. The viscosity stabilizes it. The magnetic field plays a mixed role in the fluctuation dynamics.
2) *Quantum planar regime*: In this regime, the only difference found against Case-(1) (as above) is that the magnetic field shows absurd peaks and dips in the dynamics.
3) *Classical non-planar regime*: In this regime, the only contrast against Cases-(1)-(2) is that the magnetic field stabilizes the astrofluid system.
4) *Classical planar regime*: In this regime, the only contrast against the earlier Cases is that the magnetic field destabilizes the fluctuation dynamics, and so forth.

In addition to the above, it is noteworthy that the proposed multiparametric analysis can be extensively applied to study diverse cylindrical waves excitable in elongated molecular clouds, filamentary structures, magnetized arms of spiral galaxies, and so on [28-30]. It has been seen that circumstellar discs undergo viscous evolution [50]. Circumstellar discs with masses more than 10% of the central star are more susceptible to gravitational instability [46], where more number density means more mass, and vice-versa. The mass may also increase by means of mass accretion due to rotational processes [46, 48]. Magnetic field also plays a significant role in the evolution of the protoplanetary disks [51]. The chemistry of the disc and the evolution of the grain population are affected by magnetically driven mixing [51]. The direction of migration of planets is determined by the effective viscous reaction of the disc [51]. It hereby strengthens the reliability and validity of our analysis.

It is finally admitted that our model is not completely free from basic formalism limitations. Approximate rotation input values, although judiciously used from the literature might slightly affect the pure accuracy of our numerical results. Also, consideration of non-linearity and differential rotation would actually improve the realistic applicability. There exists no sufficiency of actual astronomical stability data

needed for a complete validation and concrete reliability checkup. Against this backdrop, a refined model development on astrophysical cylindrical stability analyses with the aforesaid key factors fully considered is left here now for a future course of integrated continued study.

REFERENCES

[1] Devyatkov, V. N., Ivanov, Yu. F., Krysina, O. V., Koval, N. N., Petrikova, E. A., and Shugurov, V.V. Equipment and processes of vacuum electron-ion plasma surface engineering. *Vacuum*, 143:464-472, 2017.

[2] Koval, N. N. and Ivanov, Yu. F. Complex electron-ion-plasma processing of Aluminium surface in a single vacuum cycle. *Russian Physics Journal,* 62:1161-1170, 2019.

[3] Huang, J., Weng, S., Wang, X., Zhong, J., Zhu, X., Feng, X., Chen, M., Murakami, M., and Sheng, Z. Ion Acoustic Shock Wave Formation and Ion Acceleration in the Interactions of Pair Jets with Electron–ion Plasmas. *The Astrophysical Journal*, 931(1):36, 2022.

[4] Fermous, R., Benzekka, M., and Merriche, A. Effect of adiabatically trapped-suprathermal electrons on ion-acoustic solitons in electron-ion plasma. *Astrophysics and Space Science*, 367, 105, 2022.

[5] Liyan, L. and Jiulin, D. Ion acoustic waves in the plasma with the power-law q-distribution in nonextensive statistics. *Physica A: Statistical Mechanics and its Applications*, 387(19-20):4821-4827, 2008.

[6] Chabrier, G. and Potekhin, A. Y. Equation of state of fully ionized electron-ion plasmas. *Physical Review E***,** 58(4):4941-4949, 1998.

[7] Sah, O. P. and Manta, J. Nonlinear electron-acoustic waves in quantum plasma. *Physics of Plasmas*, 16:032304, 2009.

[8] Khan, S. A. and Masood, W. Linear and nonlinear quantum ion-acoustic waves in dense magnetized electron-positron-ion plasmas. *Physics of Plasmas,* 15:062301, 2008.

[9] El-Taibany, W. F. and Wadati, M. Nonlinear quantum dust acoustic waves in nonuniform complex quantum dusty plasma. *Physics of Plasmas*, 14:042302, 2007.

[10] Khan, S. A., Mushtaq, A., and Masood, W. Dust ion-acoustic waves in magnetized quantum dusty plasmas with polarity effect. *Physics of Plasmas,* 15:013701, 2008.

[11] Shahmansouri, M. and Alinejad, H. Effect of electron nonextensivity on oblique propagation of arbitrary ion acoustic waves in a magnetized plasma. *Astrophysics and Space Science*, 344:463–470, 2013.

[12] Shah, M. G., Hossen, M. R., and Mamun, A. A. Nonlinear propagation of positron-acoustic waves in a four component space plasma. *Journal of Plasma Physics*, 81(5): 905810517, 2015.

[13] El-Hanbaly, A. M., El-Shewy, E. K., Sallah, M., and Darweesh, H. F. Linear and nonlinear analysis of dust acoustic waves in dissipative space dusty plasmas with trapped ions. *Journal of Theoretical and Applied Physics*, 9:167-176, 2015.

[14] Borah, B., Haloi, A., and Karmakar, P. K. A generalized hydrodynamic model for acoustic mode stability in viscoelastic plasma fluid. *Astrophysics and Space Science*, 361:165, 2016.

[15] Bansal, S., Aggarwal, M., and Gill, T. S. Effect of positron density and temperature on the electron acoustic waves in a magnetized dissipative plasma. *Contributions to Plasma Physics*, 59, e201900047, 2019.

[16] Goswami, J., Chandra, S., and Ghosh, B. Shock waves and the formation of solitary structures in electron acoustic wave in inner magnetosphere plasma with relativistically degenerate particles. *Astrophysics and Space Science*, 364:65, 2019.

[17] Shatashvili, N. L., Mahajan, S. M., and Berezhiani, V. I. Nonlinear coupling of electromagnetic and electron acoustic waves in multi-species degenerate astrophysical plasma. *Physics of Plasmas*, 27:012903, 2020.

[18] Ghosh, M., Pramanik, S., and Ghosh, S. Nonlinear coherent structures of electron acoustic waves in unmagnetized plasmas. *Physics Letters A*, 396: 127242, 2021.

[19] Dasgupta, S. and Karmakar, P. K. Propagatory dynamics of nucleus-acoustic waves excited in gyrogravitating degenerate quantum plasmas electrostatically confined in curved geometry. *Scientific Reports*, 11, 19126, 2021.

[20] Dasgupta, S. and Karmakar, P. K. Relativistic ion-acoustic waves in electrospherically confined gyromagnetoactive quantum plasmas. *Chinese Journal of Physics*, 76:299-309, 2022.

[21] Andreev, P. A. Nonlinear Coupling of Electromagnetic and Spin-Electron-Acoustic Waves in Spin-polarized Degenerate Relativistic Astrophysical Plasma, arXiv:2202.11814 [physics.plasm-ph] (2022).

[22] Das, S., Atteya, A., and Karmakar, P. K. Acoustic waves in the Jovian dusty magnetosphere: a brief review and meta-analysis. *Reviews of Modern Plasma Physics*, 6:35, 2022.

[23] Khalid, M., Elghmaz, E. A., and Shamshad, L. Periodic Waves in Unmagnetized Nonthermal Dusty Plasma with Cairns Distribution. *Brazilian Journal of Physics*, 53:2, 2023.

[24] Landau, L. D. & Lifshitz, E. M. *Course of Theoretical Physics, Volume 6: Fluid Mechanics*. Pergamon Press, Oxford, England, 1959.

[25] Jan, Q., Mushtaq, A., Farooq, M., and Shah, H. A. Alfvén solitary waves with effect of arbitrary temperature degeneracy in spin quantum plasma. *Physics of Plasmas*, 25**:**082122, 2018.

[26] Haas, F. and Mahmood, S. Linear and nonlinear ion-acoustic waves in nonrelativistic quantum plasmas with arbitrary degeneracy. *Physical Review E*. 92 (5): 053112, 2015.

[27] Ali, S., Ahmad, M. & Ikram, M. Magnetoacoustic waves with effect of arbitrary degree of temperature and spin degeneracy in electron-positron-ion plasmas. *Contribution to Plasma Physics*, 60, 2019.

[28] Fan, Z. and Lou, Y-Q. Origin of the magnetic spiral arms in the galaxy NGC6946. *Nature*, 383, 800-802, 1996.

[29] Lou, Y-Q. and Xing, H-R. General polytropic magnetohydrodynamic cylinder under self-gravity. *Monthly Notices of the Royal Astronomical Society*, 456 (1): L122-L126, 2016.

[30] Lou, Y-Q. and Hu, X-Y. Gravitational collapse of conventional polytropic cylinder. *Mon. Not. Royal Astron. Soc.* **468**, 2771-2780. 2017.

[31] Strickland, M., Dexheimer, V., and Menezes, D. P. Bulk Properties of a Fermi Gas in a Magnetic Field. *Physical Review D*, 86 (12): 125032, 2012.

[32] Haas, F. *Quantum Plasmas- A hydrodynamic approach*. Springer, New York, London, 2011.

[33] Manfredi, G. How to model quantum plasmas. *Field Institute Communications*, 46:263-287, 2005.

[34] Karmakar, P. K. and Goutam, H. P. Electrostatic streaming instability modes in complex viscoelastic quantum plasmas. *Physics of Plasmas*, 23:112121, 2016.

[35] Pathan, T. A., Sutar, D. L., Pensia, R. K., and Joshi, H. Effect of rotation and quantum correction on the ion streaming instability in the magnetized dusty plasma. *Journal of Physics: Conference Series*, 1706: 012007, 2020.

[36] Kalita, D. and Karmakar, P. K. Analyzing the instability dynamics of spherical complex astroclouds in a magnetized meanfluidic fabric. *Physics of Plasmas* **27**, 022902, 2020.

[37] Karmakar, P. K. and Kalita, D. Dynamics of gravitational instability excitation in viscoelastic polytropic fluids. *Astrophysics and Space Science*, 363:239, 2018.

[38] Ferrario, L. and Wickramasinghe, D. T. Magnetic fields and rotation in white dwarfs and neutron stars. *Monthly Notices of the Royal Astronomical Society*, 356(2):615–620, 2005.

[39] Usman, S. and Mushtaq, A. Magnetorotational Instability in Quantum Dusty Plasma. *The Astrophysical Journal*, 911(1):50, 2021.

[40] Sahu, B., Sinha, A., and Roychoudhury, R. Ion-acoustic waves in dense magneto-rotating quantum plasma. *Physics of Plasmas*, 26: 072119, 2019.

[41] Fontaine, G., Brassard, P., and Bergeron, P. The Potential of White Dwarf Cosmochronology. *Publications of the Astronomical Society of the Pacific*, 113(782):409–435, 2001.

[42] Cowie, L. L. and McKee, C. F. The evaporation of spherical clouds in a hot gas. I. Classical and saturated mass loss rates. *The Astrophysical Journal*, 211:135-146, 1977.

[43] Bonitz, M., Moldabekov, Z. A., and Ramazanov, T. S. Quantum hydrodynamics for plasmas—Quo vadis?. *Phys. Plasmas*, 26:090601, 2019.

[44] Hasan, U., Masood, W., Jahangir, R., and Mirza, A. M. Oblique interaction of electrostatic nonlinear structures in relativistically degenerate dense magnetoplasmas. *Contributions to Plasma Physics*, 61, 2021.

[45] Manfredi, G., Hervieux, P-A., and Hurst, J. Fluid descriptions of quantum plasmas. *Reviews of Modern Plasma Physics*, 5: 7, 2021.

[46] Kratter, K. and Lodato, G. Gravitational Instabilities in Circumstellar Disks. *The Annual Review of Astronomy and Astrophysics*, 54:271–311, 2016.

[47] Livio, M. and Pringle, J. E. The rotation rates of white dwarfs and pulsars. *The Astrophysical Journal*, 505(1):339-343, 1998.

[48] Machida, M. N., Matsumoto, T., and Inutsuka, S. Conditions for circumstellar disc formation – II. Effects of initial cloud stability and mass accretion rate. *Monthly Notices of the Royal Astronomical Society*, 463(4):4246-4267, 2016.

[49] Chen, F. F. *Introduction to plasma physics and controlled fusion*, Plenum press, New York, London, 1984.

[50] Concha-Ramirez, F., Vaher, E. & Zwart, S. P. The viscous evolution of circumstellar discs in young star clusters. *Monthly Notices of the Royal Astronomical Society,* 482(1):732-742, 2019.

[51] Wardle, M. Magnetic fields in protoplanetary disks. *Astrophysics Space Science,* 311:35-45, 2007.